Modelling of SLM Additive Manufacturing for Magnesium Alloy

Ashish Kumar Mishra and Arvind Kumar

Abstract Light-weight materials, such as magnesium and its alloys, have excellent mechanical properties, such as high specific strength, high specific modulus, good damping ability, thermal conductivity, etc. These properties make them a potential candidate for aerospace and automotive applications. The inability of the conventional manufacturing processes to manufacture precise and high-quality magnesium parts drives the exploring of new manufacturing techniques. In this study, the feasibility of additive manufacturing of AZ91D magnesium alloy using Selective Laser Melting (SLM) process has been investigated. Numerical modelling and simulations are performed to study the melt pool shape and size evolution, temperature and velocity fields, temperature gradients and cooling rate during the SLM of AZ91D powder, and the influence of the input laser power is described. The model considers conduction heat transfers and radiation heat losses from the powder bed surface, melting and solidification and convection in the melt pool. The simulation results provide preliminary insights of the complex physical phenomena occurring during SLM of AZ91D by describing the interaction between the laser source and the magnesium powder. The temperature and the velocity field were found playing a significant role in deciding the melt pool dimensions and geometry. An attempt has been made to describe the melt pool stability by calculating the ratios of melt pool length to width and melt pool width to depth. The spatiotemporal variation of temperature shows that very large temperature gradients and cooling rates (of the order of 10^7 K/m and 10^6 K/s, respectively) can be achieved. The high cooling rates are likely to result in the development of finer microstructure and so improved mechanical properties.

A. K. Mishra · A. Kumar (✉)
Department of Mechanical Engineering, Indian Institute of Technology Kanpur, Kanpur 208016, India
e-mail: arvindkr@iitk.ac.in

1 Introduction

There is a growing interest for the use of magnesium alloys in automotive and aerospace industries, a reason behind which is their very low density compared to aluminium alloys (2/3rd of density at room temperature) and steel (2/9th of density at room temperature). The low density imparts them high specific strength and modulus, which along with their excellent thermal properties and damping characteristics make them a potential candidate for low-temperature structural applications in aerospace and automotive industries (Easton et al. 2008; Mishra 2013). However, creep susceptibility and poor surface properties limit their use as structural materials. To overcome these deficiencies, alloying elements like aluminium, zinc, manganese, etc., are usually added (Zhang et al. 2009; Zhang et al. 1998).

Casting and forming are the two conventional manufacturing techniques generally used for manufacturing magnesium alloy parts. Forming provides better mechanical properties than casting but suffers from oxidation and induced anisotropy. Castings too suffer from defects such as high porosity and gas entrapment, which deteriorate mechanical properties of the manufactured part. Moreover, difficulties in fabricating high precision parts, oxidation and huge wastage have encouraged the search for more efficient manufacturing processes. In this regard, Selective Laser Melting (SLM) based additive manufacturing can be a potential manufacturing process for magnesium alloy parts (Wei et al. 2014).

SLM is a widely used powder bed fusion based metal additive manufacturing (MAM) process. It uses a focused high energy laser beam to fully melt the powder layer particles. Full melting is commonly used for processing of pure metals and alloys, where almost the entire region of powder layer material under laser irradiation is melted along with some melting occurring in the previously solidified layer or the base layer (known as remelting). The remelting ensures proper bonding between the layers to create well-bonded high-density structures. A schematic diagram of the SLM process is shown in Fig. 1. The inherent advantages of SLM process include direct production from CAD model, excellent process capabilities and high cooling rates inside the melt pool resulting in the refined microstructure of produced parts (Wei et al. 2014), and much more. SLM fabricated metal parts have mechanical properties comparable to those of bulk materials.

SLM involves complex coupled thermal and physical phenomena, like laser–matter interaction, thermal transport, rapid melting and solidification; all significantly controlled by temperature and flow fields within the melt pool. Therefore, the knowledge of thermal behaviour during SLM is extremely important (Li and Gu 2014). Numerical modelling and simulations are extensively used in this regard, with numerous studies investigating thermal behaviour in SLM reported for common structural materials like steel (Childs and Hauser 2005; Gusarov and Smurov 2010), aluminium (Loh et al. 2015) and titanium alloys (Aggarwal et al. 2016; Li and Gu 2014).

The SLM process of magnesium alloys is challenging, due to the low melting and boiling temperatures as well as high reactivity towards oxygen and nitrogen in the powder and the molten state. Due to this, only a few experimental studies are
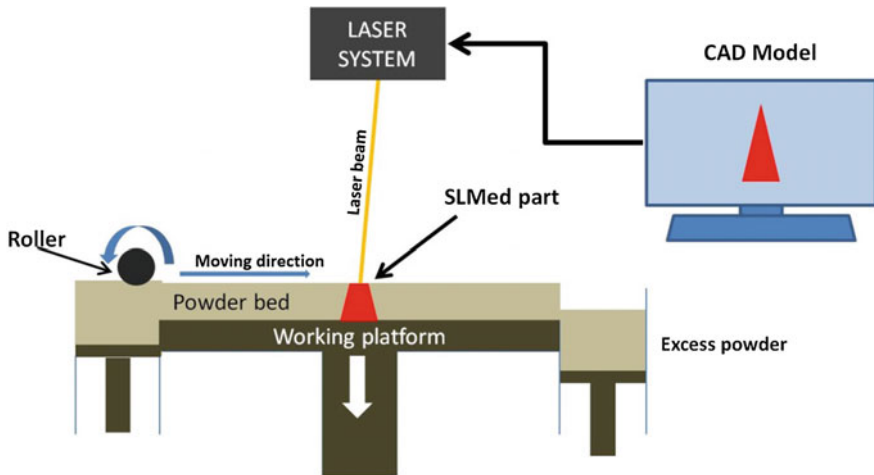
Fig. 1 Schematic diagram of SLM process

reported for SLM of magnesium alloys (Ng et al. 2011; Wei et al. 2014). Thus, numerical modelling and simulations can be used as an effective tool for detailed analysis of SLM of magnesium alloys.

In this work, a numerical model of SLM of AZ91D magnesium alloy is developed based on appropriate mathematical descriptions for the heat source, governing transport equations and boundary conditions. AZ91D is a magnesium alloy containing Al and Zn as alloying elements. Using the numerical model, simulations are performed for different laser power and results are presented for the temperature and velocity field evolution within melt pool. The melt pool characteristics (such as width, length, depth and volume), temperature gradients and cooling rate are discussed.

2 Mathematical Modelling

The model has following assumptions:

(a) The powder bed is considered as a homogeneous domain. The effect of porosity is accounted using suitable mathematical relations.
(b) Incompressible laminar flow within the melt pool.
(c) The density variation in liquid phase is approximated using the Boussinesq approximation.
(d) Material evaporation is not considered.

Simulation is performed only for half of the domain (as shown in Fig. 2) for reducing the CPU time by taking the advantage of the symmetry on the middle plane (*x*-*z* plane). The laser beam, with surface Gaussian beam profile, is applied to
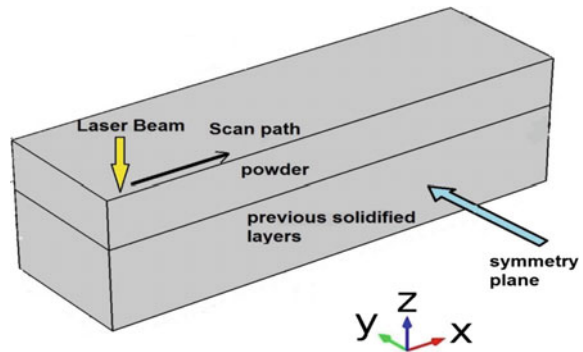
Fig. 2 Schematic of computational domain

Table 1 Process parameters for simulations

Computational domain dimensions (μm)	$500 \times 150 \times 160$
Layer thickness (μm)	60
Laser spot size (m)	100
Laser power (W)	100, 125, 150, 175, 200
Scan velocity (m/s)	1.0
Porosity (φ)	0.475

Table 2 Properties of AZ91D alloy (Friedrich and Mordike 2006)

Solidus temperature (T_S)	743 K
Liquidus temperature (T_L)	868 K
Specific heat capacity c_{PS}	1014 J/kg K (solid, 293 K)
c_{PL}	1230 J/kg K (liquid)
Thermal conductivity k_S (Solid)	72 W/m K
k_L (Liquid)	82.9 W/m K
Density (solid, 20°C) ρ_S	1810 kg/m^3
(Liquid) ρ_L	1656 kg/m^3
Latent heat of fusion L	373 kJ/kg
Dynamic viscosity μ	3×10^{-3} Pa s
Thermal expansion coefficient	2.6×10^{-5} K^{-1}
Volumetric thermal expansion coefficient (β_T)	9.541×10^{-5} K^{-1}
Temperature coefficient for surface tension ($\partial\gamma/\partial T$)	-2.13×10^{-4} N/m K
Emissivity (ε)	0.18

the top surface of the domain. The domain is divided into two layers. The top layer is considered as powder bed, while the bottom as the previously solidified layer. Both layers are of the AZ91D alloy. The process parameters used for the simulations are listed in Table 1. The thermophysical properties of the AZ91D alloy are listed in Table 2.

(A) Powder bed properties

The effect of porosity in the powder bed is accounted in thermal conductivity and density of powder bed. These quantities are calculated using following equations:

$$\rho_{\text{powder}} = \rho_{\text{s}}(1 - \varphi) \tag{1}$$

$$k_{\text{powder}} = k_{\text{s}}(1 - \varphi) \tag{2}$$

(B) Governing transport equations.

(1) Continuity equation:

$$\vec{\nabla} \cdot \rho\vec{u} = 0 \tag{3}$$

(2) Momentum conservation equation:

$$\frac{\rho\partial\vec{u}}{\partial t} + (\rho\vec{u} \cdot \nabla)\vec{u} = -\nabla p + \nabla \cdot \left(\mu\left(\nabla\vec{u} + (\nabla\vec{u})^T\right)\right) + \vec{F}, \tag{4}$$

where $\vec{F}$ is a source term used to take account of the buoyancy forces and the mushy region flow resistance. The symbols ρ, $\vec{u}$, μ and p represent density, velocity field, dynamic viscosity and dynamic pressure, respectively.

$$\vec{F} = \overrightarrow{F_{\text{n}}} + \overrightarrow{F_{\text{s}}} \tag{5}$$

$$\overrightarrow{F_{\text{s}}} = \frac{C(1 - f_{\text{L}})^2}{b + f_{\text{L}}^3}\vec{u}, \tag{6}$$

where f_{L} represents the liquid fraction, C and b are constants used for flow within the two-phase zone.

The source term $\overrightarrow{F_{\text{n}}}$ is given as

$$\overrightarrow{F_{\text{n}}} = \rho\vec{g}\beta_{\text{T}}(T - T_{\text{ref}}) \tag{7}$$

(3) Energy conservation equation:

$$\rho c_{\text{P}}\frac{\partial T}{\partial t} + \rho c_{\text{P}}\vec{u} \cdot \nabla T = \nabla \cdot (k\nabla T), \tag{8}$$

where ρ, c_P and k are given by following relations,

$$\rho = (1 - f_L)\rho_S + f_L\rho_L \tag{9}$$

$$c_P = \frac{1}{\rho}\{(1 - f_L)\rho_S c_{PS} + f_L\rho_L c_{PL}\} + \frac{L\partial\alpha_m}{\partial T} \tag{10}$$

$$k = (1 - f_L)k_S + f_L k_L \tag{11}$$

$$\alpha_m = \frac{1}{2}\frac{(f_L\rho_L - (1 - f_L)\rho_S)}{(f_L\rho_L + (1 - f_L)\rho_S)} \tag{12}$$

In Eqs. (9), (10), (11) and (12), the properties k_S and ρ_S are taken as given in Eqs. (1, 2) for the powder domain and for the solid domain as given in Table 2, while c_{PS} is taken as constant for both the powder and the solid domain, as given in Table 2.

(C) Boundary conditions
   At top surface

$$k\frac{\partial T}{\partial z} = q_{in} - h_c(T - T_\infty) - \varepsilon\sigma(T^4 - T_\infty^4) \tag{13}$$

$$q_{in} = \frac{2\varepsilon P}{\pi R^2}\exp\left(-\frac{2((x - Vt)^2 + y^2)}{R^2}\right), \tag{14}$$

where q_{in} is input heat flux and R is the laser spot radius. The symbols ε, σ, T_∞ and h_c represent emissivity, Stefan–Boltzmann constant, ambient temperature and convection coefficient, respectively. The velocity boundary condition at the top surface is given as

$$-\frac{\mu\partial u}{\partial z} = \frac{\partial\gamma}{\partial T}\left(\frac{\partial T}{\partial x}\right) \tag{15}$$

$$-\frac{\mu\partial v}{\partial z} = \frac{\partial\gamma}{\partial T}\left(\frac{\partial T}{\partial y}\right), \tag{16}$$

where γ is surface tension.

The domain boundaries, except plane of symmetry and top boundary, are considered adiabatic.

3   Results and Discussion

Figure 3 shows the temperature and melt pool evolution with time for laser power $P = 100$ W. The colour map shows the temperature field, while the curved boundary represents the melt pool. The temperature in the domain starts increasing with time as the laser heating starts. The melting starts once the temperature exceeds the solidus temperature, forming a melt pool which travels along the scan direction following the moving laser beam. The melt pool grows rapidly during initial time, as shown in Fig. 3 at 200 and 300 μs. However, it achieves a quasi-steady state after some time.

This is shown in Fig. 3 at 700 μs where no change is observed in the melt pool size and the temperature till 900 μs. The maximum temperature in the computational domain is observed in the central region of the melt pool, where the beam intensity is the highest. This maximum domain temperature with time is plotted in Fig. 4, which gives a glimpse of temperature field evolution within computational domain. The maximum domain temperature increases rapidly (in less than 20 μs) to 1600 K and then the further increase in the temperature slows down. After $t = 500$ μs, the variations are small enough (largest variation in maximum domain temperature is 2.6% after $t = 500$ μs) to consider the process attaining a quasi-steady state. This trend of rapidly reaching the maximum temperature and then remaining stable around the same value can be attributed to the very large thermal conductivity of the AZ91D alloy which facilitates rapid thermal transport and dissipation.

A very high velocity of the order of 3.65 m/s is induced (due to Marangoni convection) in the melt pool at 100 W. Such high velocity greatly enhances lateral heat transfer and mixing in melt pool (through convection) and results in wider melt pools. Combined with the very large thermal conductivity of the alloy, it resulted in deeper melt pool. However, despite the deeper penetration of melt pool and longer growth duration, no remelting is seen at 100 W. Remelting is defined as the melting of previous deposited/base layers and is critical to ensure manufacturing of well-bonded high-density parts.

Melt pool dimensions (length, width and depth) increase with time during the initial stage, but as the melt pool becomes steady the dimensions of the melt pool become stable. The same is illustrated by the plot of melt pool volume with time, plotted in Fig. 5. Confirming to the previous discussions, the melt pool grows initially as the volume increases linearly from 100 to 200 μs. After 200 μs, the rate of growth of the melt pool volume slows down and continues till around 680 μs after which the growth stops and melt pool becomes quasi-steady. The steady-state melt pool volume is found as 3.75×10^{-13} m^3 at 100 W laser power. From Figs. 4 and 5, it is evident that the melt pool becomes quasi-steady after $t = 700$ μs, and accordingly, the temperature, the flow velocity and the melt pool characteristics do not experience any significant variation subsequently.

Figure 6 illustrates the effect of increasing laser power on the melt pool. The results are shown at 800 μs when the quasi-steady state is already achieved.
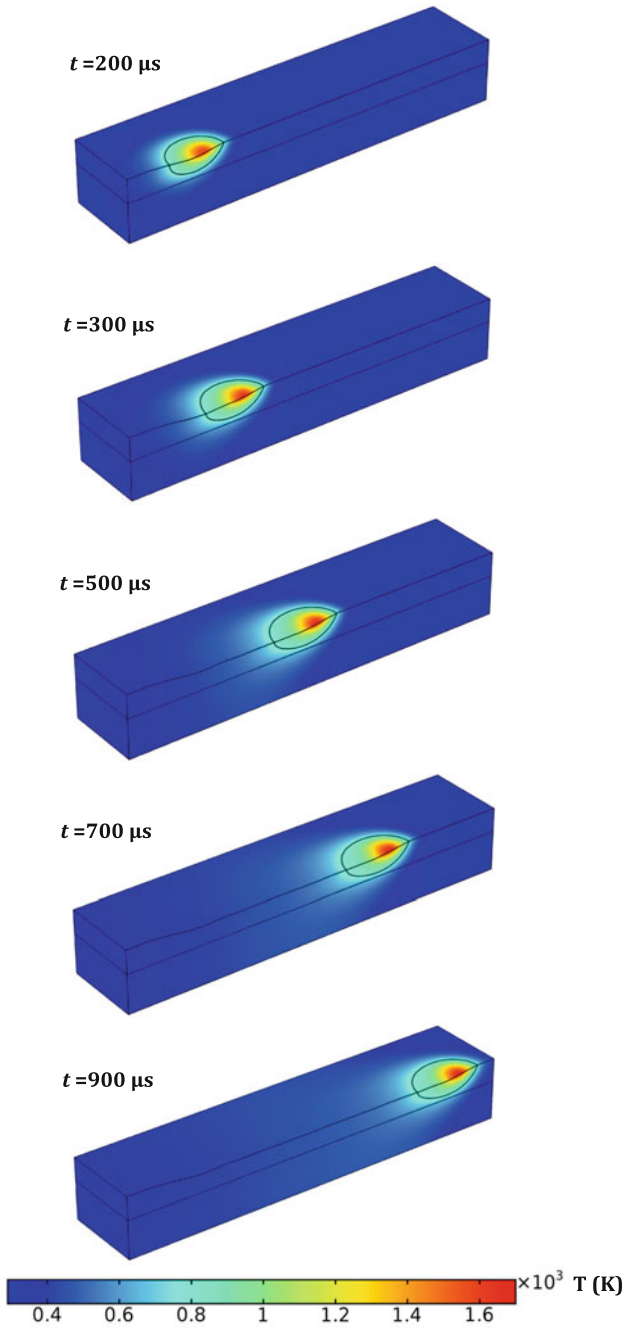
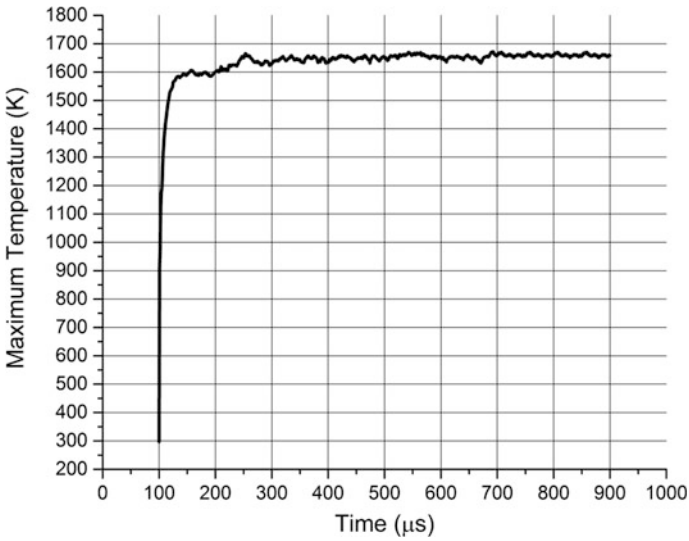**Fig. 3** Melt pool evolution with time at $P = 100$ W

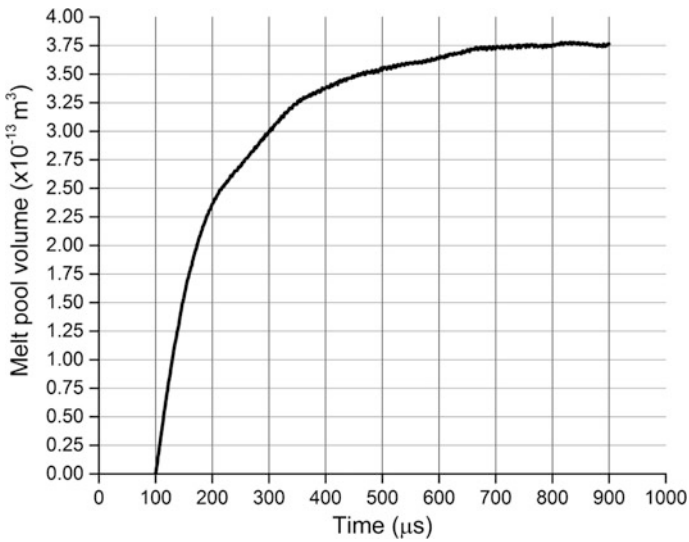**Fig. 4** Maximum domain temperature with time at $P = 100$ W

Fig. 5 Melt pool volume with time at $P = 100$ W

The comparison of melt pool length, width, depth, maximum temperature and velocity corresponding to these results is discussed later. The colour plot represents the temperature distribution while arrows show the velocity field. The velocity field is outwards, typical to the Marangoni flow for the molten metals. The maximum
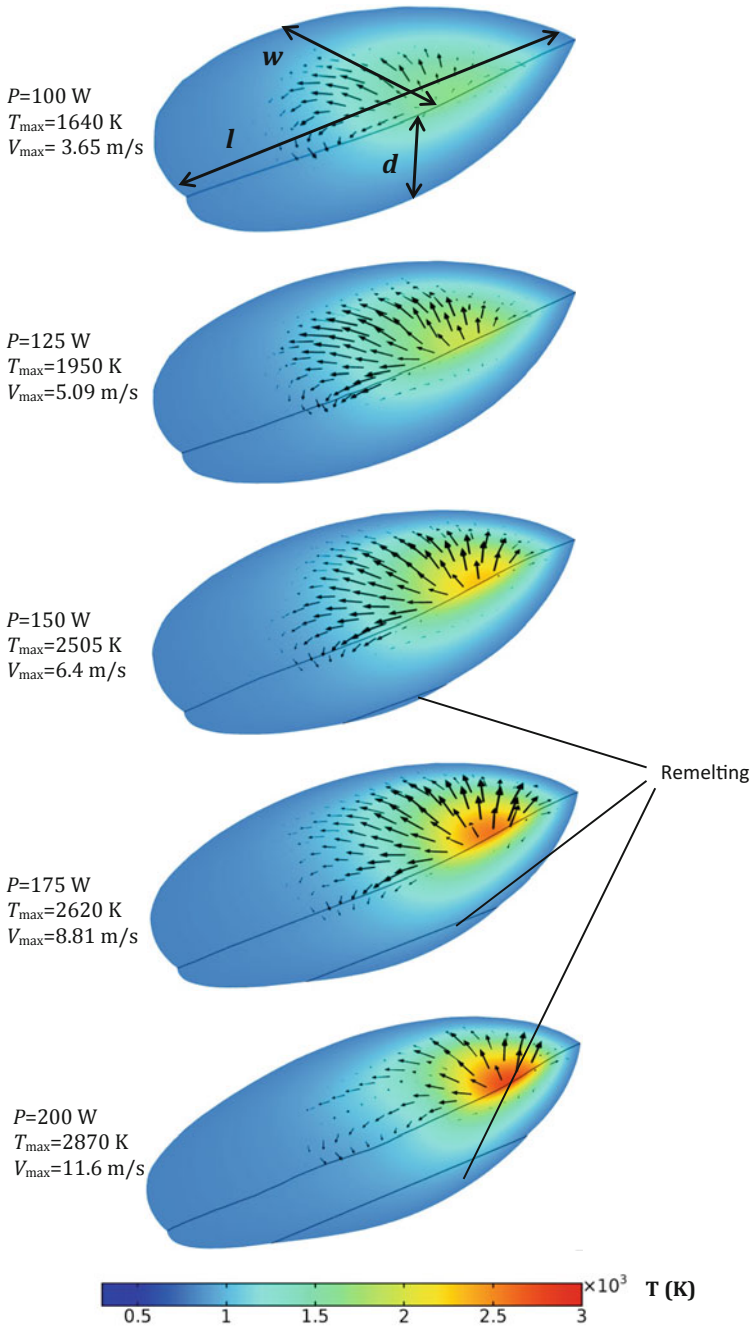
Fig. 6 Melt pool comparison for different laser power ($t = 800$ μs)

temperature and flow velocity values increase as the laser power increases from 100 to 200 W. The flow velocity within melt pool increases because the temperature distribution becomes steeper resulting in stronger Marangoni convection as the laser power increases. The maximum temperature and the maximum velocity in melt pool increase drastically respectively from 1640 K, 3.65 m/s at 100 W to 2870 K, 11.6 m/s at 200 W. However, such high temperatures and high velocities will not be present in reality as there will be evaporation and the region which experiences such high velocities will eventually get evaporated. Still, a maximum flow velocity of around 5 m/s is expected to be induced in reality at 200 W.

The melt pool dimensions (length, half width and depth) are found increasing as the laser power is increased (Fig. 7), owing to the higher temperatures and enhanced heat transfer at increased laser power as discussed before. The increase in the melt pool half width (w) is more linear in trend than the melt pool length (l) or the depth (d). The melt pool length increases much rapidly when the laser power is increased, showing the effect of the very high thermal conductivity of the solidified material past the melt pool resulting in more diffusion of thermal energy (both the transported energy and the evolved latent heat of solidification) over longer distances. The melt pool depth increases due to increased convection within melt pool at increased laser power, which causes the molten metal to penetrate deeper in the powder layer and eventually remelting starts to occur in the previously solidified/base layer also at 150 W. Considerable remelting is observed at laser power higher than 150 W, suggesting the use of higher laser power to obtain sufficient remelting. However, more evaporation occurs at higher laser powers and so there is a trade-off in the selection of laser power so as to prevent excess evaporation and to ensure sufficient remelting.

The same is visible in the plot of melt pool volume versus laser power, shown in Fig. 8. The melt pool volumes are plotted when they had achieved the quasi-steady state. The melt pool volume is found to increase nonlinearly with the laser power,

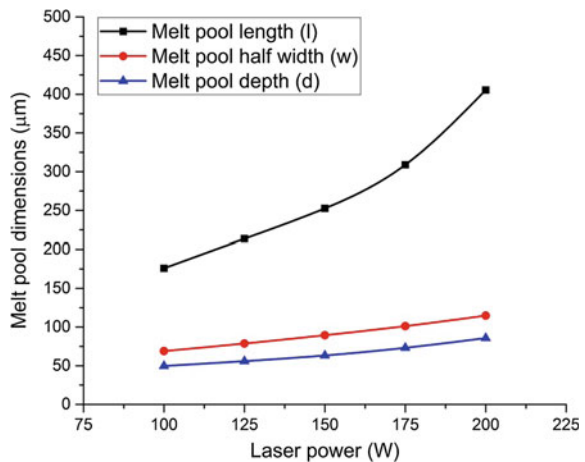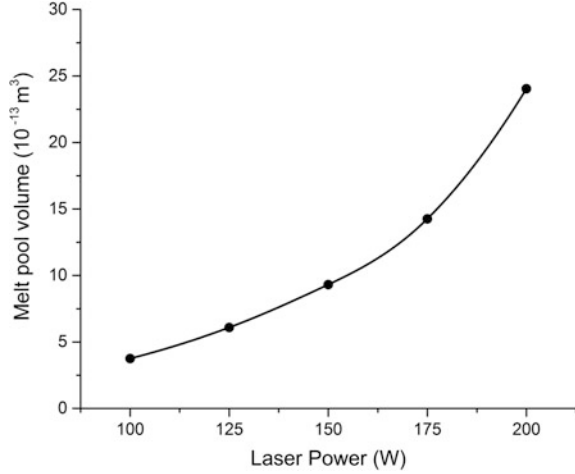**Fig. 7** Variation of melt pool dimensions for different laser power

Fig. 8 Melt pool volume for
different laser power at
$t = 800\ \mu s$

from 7.5×10^{-13} m^3 at 100 W to 4.8×10^{-12} m^3 at 200 W. An empirical relationship between the quasi-steady melt pool volume and the laser power is proposed, as given in the following

$$\text{Melt pool volume} = (0.9522 + 0.8777 \exp(0.01988P)) \times 10^{-13} \text{m}^3 \qquad (17)$$

where P is the value of input laser power in Watt.

The melt pool aspect ratio (length/width) and the ratio of melt pool width to depth are the key attributes for the stability of the melt pool during SLM. These are plotted in Figs. 9, 10 for different laser power. The values were calculated from the quasi-steady melt pool results. In the present case, the aspect ratio ($l/(2w)$) is found increasing from 1.28 at 100 W to 1.77 at 200 W. The melt pool width to depth ratio ($2w/d$), on the other hand, was found quite high (nearly twice the aspect ratio). It increased from 2.78 at 100 W to 2.83 at 150 W and then decreased to 2.68 at 200 W. Such high values indicate shallower melt pools typically resulted from the outwards flow of molten metal in melt pool (Marangoni flow). The decrease in the width to depth ratio after 150 W is due to the penetration of melt pool in the bulk solid material layer below the powder layer, where the very high thermal conductivity resulted in increased heat transfer and hence deeper melt pools. Higher values of these ratios should be undesirable in order to keep the melt pool stable and hence a careful selection of input process parameters is required.

An attempt is made to propose a mathematical correlation between these ratios and the input laser power through curve fitting. The melt pool aspect ratio ($l/(2w)$) versus laser power plot was found to follow a cubic polynomial of the form

$$\frac{l}{2w} = a_0 + a_1 P + a_2 P^2 + a_3 P^3 \qquad (18)$$

Fig. 9 Melt pool aspect ratio (*l/2w*) for different input laser power
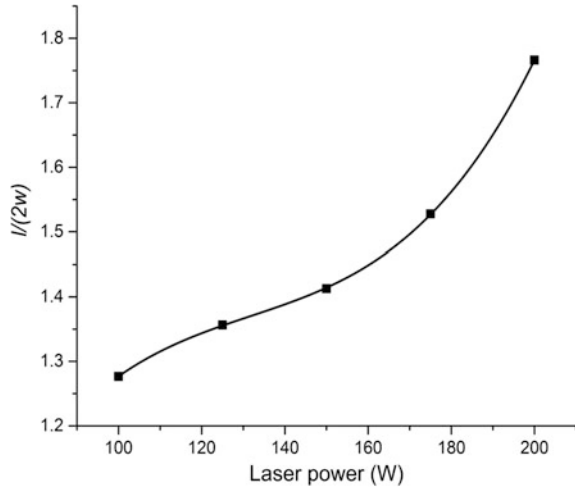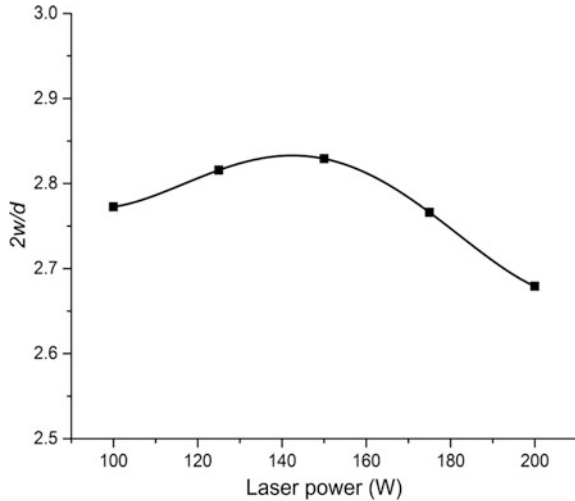

Fig. 10 Melt pool width to depth ratio (*2w/d*) for different input laser power

The melt pool width to depth ratio is found to follow a quartic polynomial of the form

$$\frac{2w}{d} = a_0 + a_1 P + a_2 P^2 + a_3 P^3 + a_4 P^4, \tag{19}$$

where P is the value of input laser power (in Watt). The value of coefficients of above polynomials is listed in Table 3.

The temperature gradient and the temperature–time history play a significant role in the development of melt pool, residual stresses and distortion in the

Table 3 Coefficients of the polynomial expressions

Coefficients	$l/(2w)$	$2w/d$
a_0	−0.7075	6.7072
a_1	0.043	−0.1214
a_2	−3.1 x 10^{-4}	0.00135
a_3	7.8437 x 10^{-7}	−6.31457 x 10^{-6}
a_4	–	1.0578 x 10^{-8}

manufactured part and hence its study has significant importance. A detailed discussion of the same is out of the scope of this work, and only a brief discussion is presented here to highlight the effect of laser power on the temperature gradient and the temperature–time history. The locations of line and point data sets used to show temperature gradient and temperature–time history are depicted in Fig. 11. Figure 12 shows temperature variation along the length, width and depth (EAB, AC and AD in Fig. 11), respectively for different laser power at time $t = 500$ μs. Very large temperature gradients (of the order of 10^7 K/m) are induced in the SLM process during both heating and cooling. From the plots, it is evident that the temperature gradients along all three directions (T'_x, T'_y and T'_z) increase with increasing the laser power. The temperature gradient is larger at the melting front than at the solidification front (Fig. 12a), the reason of which is the very high thermal conductivity of the bulk solid after the solidification front which results in quick heat diffusion over longer distances. Also, a notable point in Fig. 12a is the delayed temperature fall witnessed near the solidification front, shown by the inflexion in the plot towards the solidification front (region between 250 to 400 μm). The delayed fall in temperature is resulted by the evolution of the latent heat of solidification at the solidification front, which does not allow the temperature to fall continuously. The temperature distribution along the width (AC in Fig. 11) closely resembles the Gaussian distribution of incident beam energy. The temperature gradient T'_y, at a particular laser power, first increases and then decreases while moving away from the beam centre; and eventually vanishing at the outer wall of the domain. The increase in the temperature gradient components T'_x and T'_y with increasing laser power explains the increase in the melt pool flow velocity with laser power. The temperature distribution along the depth, i.e. AD in Fig. 11, shows the exponential decrease while moving away from the top surface (which is irradiated by the laser beam). The temperature gradient component T'_z too is very high near the top surface and continues to decrease exponentially along the depth.

The cooling rate is another important attribute in determining the end product microstructure and mechanical properties. Here, to determine the cooling rate, the temperature at a particular point (point 'A', Fig. 11) is plotted with respect to time (see Fig. 13). It is evident that during SLM, as the laser beam passes through a point

Fig. 11 Locations of line and point data sets used to show temperature gradient and temperature–time history. The location of point A is (500, 0, 160 μm)
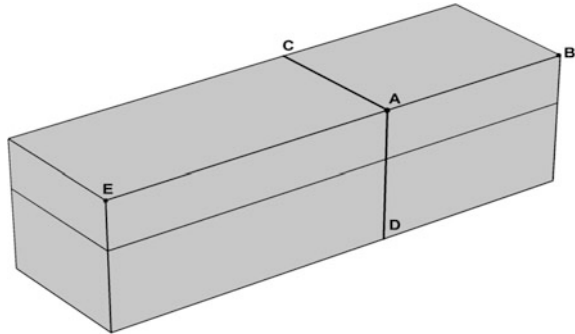
(point 'A' in this case) the temperature rises and then falls rapidly resulting in very high heating and cooling rates of the order of 10^6 K/s in the melt pool. This can be attributed to the very small time of interaction of laser beam with the material (defined as the laser beam spot diameter divided by laser beam scan speed). Such high cooling rates in the melt pool give rise to the nucleation of very fine grains (rapid solidification), which along with the very small time available (interaction time) for mixing and grain growth result in finer microstructure and consequently superior mechanical properties when compared to the conventional manufacturing.

A noticeable aspect in Fig. 13 is the occurrence of prolonged arrest in the temperature drop during cooling when the melt pool is about to pass the point A, visible from the point of inflexion in the *T-t* curves after 600 μs. This is the effect of the evolution of the latent heat of solidification at the solidification front which prevents the temperature from falling for a longer duration. The cooling rate in the solidified material is, however, much smaller implying that further grain growth will not occur once the material is solidified. A detailed analysis of solidification microstructure and grain growth needs experimental analysis and hence is not attempted here.

Overall, it was found from the current results that the temperature and the resulting flow velocity field increase with time till the quasi-steady state is achieved, after which no significant variation was observed. These quantities were also found increasing when the value of the input laser power was increased. The melt pool dimensions and geometry were also found dependent on temperature and molten metal velocity and increased with increasing the laser power. This was also reflected in the plot of melt pool volume versus laser power which showed an exponential increase. The temperature gradients and cooling rates were found very high (of the order of 10^7 K/m and 10^6 K/s, respectively) with the latent heat evolution causing some delay in cooling in the solidification zone.

Fig. 12 Temperature
distribution along **a** length
(EAB), **b** width (AC) **c** depth
(AD) for different laser power
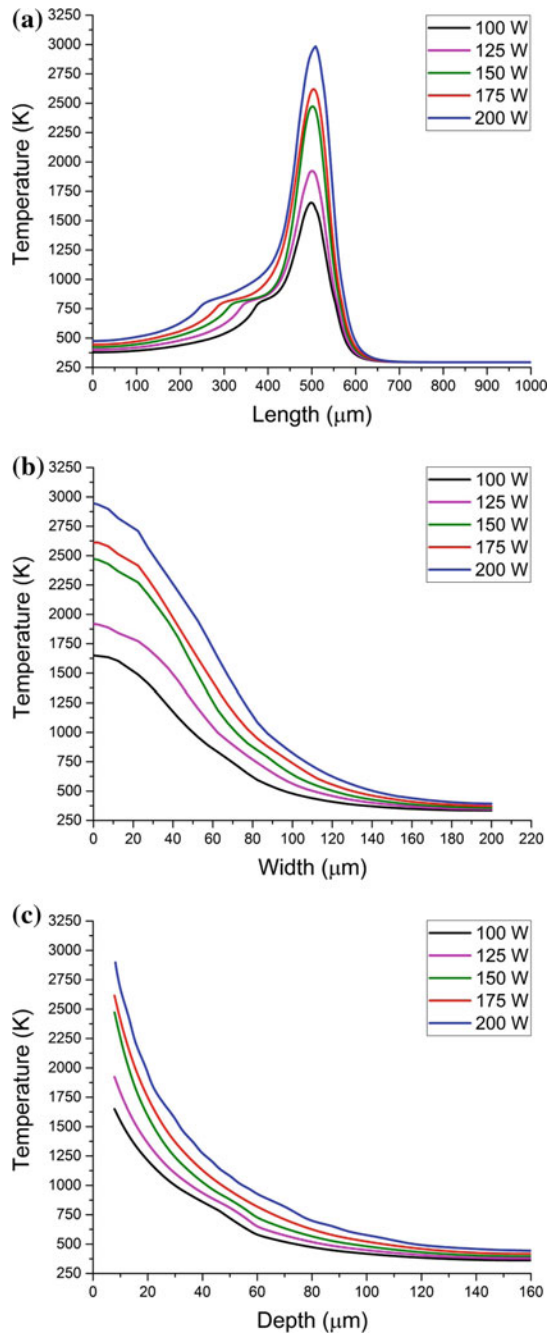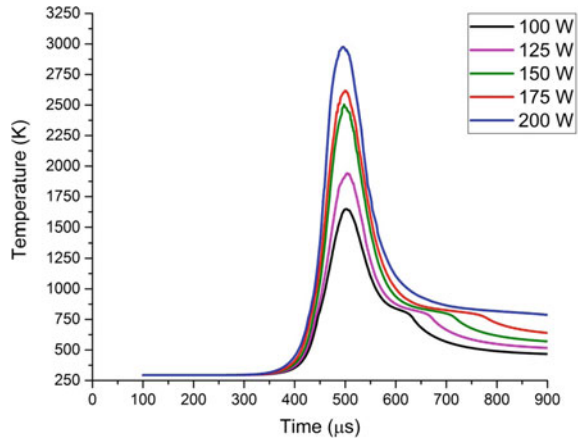at $t = 500$ μs

Fig. 13 Temperature–time variations at point A for different laser power

4 Conclusion

This work reports a numerical model of SLM for AZ91D magnesium alloy and simulation results for various input laser power values. Experimental studies for additive manufacturing of magnesium alloys are greatly needed and irreplaceable, then numerical simulations alone due to very little studies in this field. Nevertheless, it was found that such numerical studies can provide preliminary insights of the complex physical phenomena occurring during SLM AZ91D and their dependence on the key process parameters, such as laser power. The temperature and the resulted velocity field of molten metal were found playing a significant role in heat transfer and were governing factors in deciding the melt pool dimensions and geometry. Both the temperature and flow velocity were found increasing when the value of input laser power was increased, showing their greater dependence on the input energy. The high velocities in conjunction with the very high thermal conductivity of the material result in enhanced heat transfer in the domain which results into larger melt pool. The high velocities, though, may also cause penetration of molten metal in the powder bed and compromise the melt pool stability. The melt pool dimensions were found increasing when the laser power increased, which was reflected by the melt pool volume which increases exponentially with increase in laser power. An attempt was made to briefly study the melt pool stability by calculating the ratios of melt pool length to width and melt pool width to depth. The melt pool width to depth ratio is much higher (2.6–2.8) showing the formation of shallow melt pools. This also meant that the melt pool is prone to destabilise. The spatiotemporal variation of temperature shows that very large temperature gradient and cooling rates (of the order of 10^7 K/m and 10^6 K/s, respectively) can be achieved. Such high values can result in significant residual stresses and distortion in the manufactured part. The high cooling rates are likely to result in the development of finer microstructure and so improved mechanical properties. However, the need of a detailed experimental analysis of temperature

gradients and cooling rates and their effect is felt greatly in order to support the observations made through numerical simulations.

References

Aggarwal, A., H. Khoont, and A. Kumar. 2016. Investigation of transport phenomena in selective laser melting of Ti-6Al-4 V. In *3rd Annual International Conference on Materials Science, Metal & Manufacturing*, 2016, Singapore.

Childs, T., and Hauser, C. 2005. Raster scan selective laser melting of the surface layer of a tool steel powder bed. *Proceedings of the Institution of Mechanical Engineers, Part B: Journal of Engineering Manufacture* 219: 379–384.

Easton, M., A. Beer, M. Barnett, C. Davies, G. Dunlop, Y. Durandet, S. Blacket, T. Hilditch, and P. Beggs. 2008. Magnesium alloy applications in automotive structures. *The Journal of The Minerals, Metals & Materials Society* 60 (11): 57–62.

Friedrich, H.E., and B.L. Mordike. 2006. *Magnesium technology: Metallurgy, design data, applications*. Berlin, Heidelberg: Springer.

Gusarov, A., and I. Smurov. 2010. Modelling the interaction of laser radiation with powder bed at selective laser melting. *Physics Procedia* 5: 381–394.

Li, Y., and D. Gu. 2014. Thermal behaviour during selective laser melting of commercially pure titanium powder: Numerical simulation and experimental study. *Additive Manufacturing* 1–4: 99–109.

Loh, L., C. Chua, W. Yeong, M. Mapar, S. Sing, Z. Liu, and D. Zhang. 2015. Numerical investigation and an effective modelling on the Selective Laser Melting (SLM) process with aluminium alloy 6061. *International Journal of Heat and Mass Transfer* 80: 288–300.

Mishra, S. 2013. Magnesium alloys in aerospace applications. *NCAIR newsletter* 3 (2): 7–9.

Ng, C.C., M.M. Savalani, M.L. Lau, and H.C. Man. 2011. Microstructure and mechanical properties of selective laser melted magnesium. *Applied Surface Science* 257: 7447–7454.

Wei, K., M. Gao, Z. Wang, and X. Zeng. 2014. Effect of energy input on formability, microstructure and mechanical properties of selective laser melted AZ91D magnesium alloy. *Material Science and Engineering A* 611: 212–222.

Zhang, Z., A. Couture, and A. Luo. 1998. An investigation of the properties of Mg-Zn-Al alloys. *Scripta Materialia* 39 (1): 45–53.

Zhang, E., D. Yin, L. Xu, L. Yang, and K. Yang. 2009. Microstructural, mechanical and corrosion properties and biocompatibility of Mg-Zn-Mn alloys for biomedical application. *Material Science and Engineering* C29: 987–993.